JCI insight

RESEARCH ARTICLE

Multimodal imaging guides surgical management in a preclinical spinal implant infection model

Stephen D. Zoller,[1] Howard Y. Park,[1] Tove Olafsen,[2] Charles Zamilpa,[2] Zachary D.C. Burke,[1] Gideon Blumstein,[1] William L. Sheppard,[1] Christopher D. Hamad,[3] Kellyn R. Hori,[3] Jen-Chieh Tseng,[4] Julie Czupryna,[4] Craig McMannus,[4] Jason T. Lee,[2] Mafalda Bispo,[5] Francisco Romero Pastrana,[5] Elisa J.M. Raineri,[5] Jeffery F. Miller,[6,7] Lloyd S. Miller,[8,9,10] Jan Maarten van Dijl,[5] Kevin P. Francis,[1,4] and Nicholas M. Bernthal[1]

[1]Department of Orthopedic Surgery, David Geffen School of Medicine at UCLA, Santa Monica, California, USA. [2]Crump Institute for Molecular Imaging, Department of Molecular and Medical Pharmacology, UCLA, Los Angeles, California, USA. [3]David Geffen School of Medicine at UCLA, Los Angeles, California, USA. [4]PerkinElmer, Hopkinton, Massachusetts, USA. [5]Department of Medical Microbiology, University of Groningen, University Medical Center Groningen, Groningen, Netherlands. [6]California NanoSystems Institute, UCLA, Los Angeles, California, USA. [7]Department of Microbiology, Immunology, and Molecular Genetics, David Geffen School of Medicine, UCLA, Los Angeles, USA. [8]Department of Orthopaedic Surgery, [9]Department of Dermatology, and [10]Division of Infectious Disease, Department of Medicine, Johns Hopkins University School of Medicine, Baltimore, Maryland, USA.

Spine implant infections portend disastrous outcomes, as diagnosis is challenging and surgical eradication is at odds with mechanical spinal stability. Current imaging modalities can detect anatomical alterations and anomalies but cannot differentiate between infection and aseptic loosening, diagnose specific pathogens, or delineate the extent of an infection. Herein, a fully human monoclonal antibody 1D9, recognizing the immunodominant staphylococcal antigen A on the surface of *Staphylococcus aureus*, was assessed as a nuclear and fluorescent imaging probe in a preclinical model of *S. aureus* spinal implant infection, utilizing bioluminescently labeled bacteria to confirm the specificity and sensitivity of this targeting. Postoperative mice were administered 1D9 probe dual labeled with 89-zirconium (^{89}Zr) and a near infrared dye (NIR680) (^{89}Zr-NIR680-1D9), and PET-CT and in vivo fluorescence and bioluminescence imaging were performed. The ^{89}Zr-NIR680-1D9 probe accurately diagnosed both acute and subacute implant infection and permitted fluorescent image-guided surgery for selective debridement of infected tissue. Therefore, a single probe could noninvasively diagnose an infection and facilitate image-guided surgery to improve the clinical management of implant infections.

Conflict of interest: JCT, JC, CM, and KPF report that they are employees of PerkinElmer, a manufacturer of optical and PET imaging equipment. LSM reports that he has received grant support from MedImmune, Pfizer, Moderna Therapeutics, Regeneron Pharmaceuticals, and Boehringer Ingelheim and consulting fees from Integrated BioTherapeutics, related to *Staphylococcus aureus* vaccines and therapeutics. JMVD reports that he has filed a patent application (WO2015/088346) on the use of 1D9, which is owned by his employer University Medical Center Groningen. NMB reports that he has received consulting fees from Zimmer Biomet, Bonesupport, Daiichi Sankyo, and Onkos and that he is a board or committee member of the Musculoskeletal Tumor Society and Orthopaedic Research and Education Foundation.

Submitted: September 25, 2018
Accepted: January 9, 2019
Published: February 7, 2019

Reference information:
JCI Insight. 2019;4(3):e124813.
https://doi.org/10.1172/jci.insight.124813.

Introduction

Infection is a devastating complication after orthopedic surgery, as surgical implants provide a safe haven for recalcitrant, biofilm-associated infections. This is particularly evident in spinal surgery, as infection can lead to destabilization of the spinal column, multiple reoperations, disability, paralysis, and even death (1, 2). Despite decades of efforts aimed at "best practices" (3, 4), implant infection continues to occur after 2%–10% of spine surgeries (1, 5–8). *Staphylococcus aureus* is the most common pathogen; it is capable of forming biofilms on the implants and, thereby, blocking immune responses and antibiotic activity (9–11). While the majority of biofilm-associated implant infections require removal of the implants, this is often not possible with spinal implants, because they are necessary for mechanical stability of the spine (12–14). As a result, improved diagnosis and treatment of spinal infections has the potential to greatly improve patient outcomes.

Specifically, distinguishing between infectious and aseptic etiologies and determining the inciting pathogen are extremely challenging. Following an initial spinal surgery, patients frequently return with continued pain, which is concerning as a possible sign of infection. Currently available x-ray, CT, and MRI modalities only provide anatomical information regarding altered bone and tissue surrounding the

implants and have limited utility due to metal artifacts that obscure the bone-implant interface (15–18). Clinical algorithms that combine PET imaging with fluorine-18-fluorodeoxyglucose (^{18}F-FDG) can be employed (19), but ^{18}F-FDG accumulates at sites of both infectious and aseptic inflammation (20–22). Therefore, the decision regarding appropriate management, including surgery and local and systemic antibiotics, is often made empirically without accurate information (19). This has the unwanted consequence of subjecting patients to "unguided" surgical debridement that is either insufficient (failing to clear the infection) or excessive (removing healthy tissue that affects function of the spine). Although intraoperative microbiologic cultures are informative, results take days (23, 24), and the empiric local and systemic antibiotic might not have efficacy against the causative organism.

To increase the specificity of pathogen diagnosis, the fully human monoclonal antibody 1D9 that targets the immunodominant staphylococcal antigen A (IsaA) of *S. aureus* (25, 26) labeled with a radionuclide (89-zirconium [^{89}Zr]) or a near-infrared fluorophore (NIR680) was previously effective in noninvasively diagnosing a *S. aureus* soft tissue infection in mice using PET-CT or in vivo fluorescence imaging (FLI), respectively (26). However, it is unclear so far whether the 1D9 probe could facilitate diagnosis as well as guide treatment of a more complex biofilm-associated *S. aureus* implant infection. Therefore, we investigated the 1D9 probe (25, 26), dual labeled with ^{89}Zr and the NIR680 dye (i.e., ^{89}Zr-NIR680-1D9), as a multimodal noninvasive approach to distinguish septic from aseptic inflammation, diagnose *S. aureus* infection specifically, and facilitate intraoperative image-guided selective debridement of fluorescently labeled infected tissue in a preclinical *S. aureus* spinal implant infection model that utilized bioluminescently labeled bacteria to further confirm the specificity and sensitivity of this targeting probe (27).

Results

1D9 fluorescent probe to detect an S. aureus in vitro biofilm. First, to determine whether the 1D9 antibody probe could detect *S. aureus* bacteria in a biofilm, in vitro–grown biofilms of *S. aureus* strains Xen36, SH1000, and MS001, a Δ*isaA* mutant of *S. aureus* (as a control because it does not express the 1D9 target), were incubated with 1D9 labeled with Alexa Fluor 555, and the selective targeting of this probe was determined by confocal microscopy (Figure 1 and Supplemental Figure 1; supplemental material available online with this article; https://doi.org/10.1172/jci.insight.124813DS1). The 1D9–Alexa Fluor 555 probe readily detected *S. aureus* Xen36 and SH1000 in the in vitro biofilms. In comparison there was minimal background labeling in the Δ*isaA* mutant, which was likely due to nonspecific binding of the antibody by the Fc-binding factors Spa and Sbi (26). These data revealed highly effective binding of the 1D9 antibody to in vitro *S. aureus* biofilms.

Mouse model of spinal implant S. aureus infection using bioluminescence imaging. To evaluate the ability of conventional ^{18}F-FDG PET-CT versus ^{89}Zr-NIR680-1D9 PET-CT or in vivo FLI to detect an in vivo biofilm infection, an established mouse model of *S. aureus* spinal implant infection was employed (27). Spinal surgery with implantation of an L-shaped implant and inoculation with bioluminescent *S. aureus* (Xen36 strain) was performed in conjunction with in vivo bioluminescence imaging (BLI) on postoperative days (POD) 0, 1, 3, 5, and 7 (Figures 2 and 3). The mean in vivo BLI signal of Xen36 bacterial burden was significantly higher in infected mice compared with that in sterile mice at all POD time points ($P < 0.05$). On POD 7, the in vivo BLI signals were approximately 10-fold higher in infected versus sterile mice. This model was used for further experiments, as schematically represented in Figure 2A with different colored flags and Figure 2B with the illustration of the process. Specifically, the experiments included the spinal implant surgery and *S. aureus* inoculation (Figure 2A, red), in vivo BLI imaging to monitor bacterial burden (Figure 2A, blue), administration of ^{89}Zr-NIR680-1D9 and PET-CT imaging (Figure 2A, green) or administration of ^{18}F-FDG and PET-CT imaging (Figure 2A, orange), and FLI with or without image guided surgery (Figure 2A, yellow) and CFU enumeration (Figure 2A, purple).

^{18}F-FDG PET-CT imaging of an S. aureus biofilm infection in vivo. Validating data demonstrated that conventional ^{18}F-FDG PET-CT imaging could delineate infected from sterile postoperative wounds at POD 7 (Supplemental Figures 2 and 3). Further analysis showed that the ^{18}F-FDG mean standard uptake value (SUV_{mean}) in infected mice ($n = 11$) or sterile mice ($n = 4$) was significantly different during the acute infection on POD 7 (SUV_{mean} 1.54 ± 0.23 versus 0.88 ± 0.10; $P < 0.001$) and chronic infection on POD 22 (SUV_{mean} 0.98 ± 0.25 versus 0.63 ± 0.11; $P < 0.05$) (Figure 4, A–H). Both infected and sterile mice had decreased ^{18}F-FDG accumulation from days 7 to 22, with differences being less pronounced on day 22, highlighting the challenges of using ^{18}F-FDG and PET/CT imaging to distinguish between infection and sterile inflammation. It should be

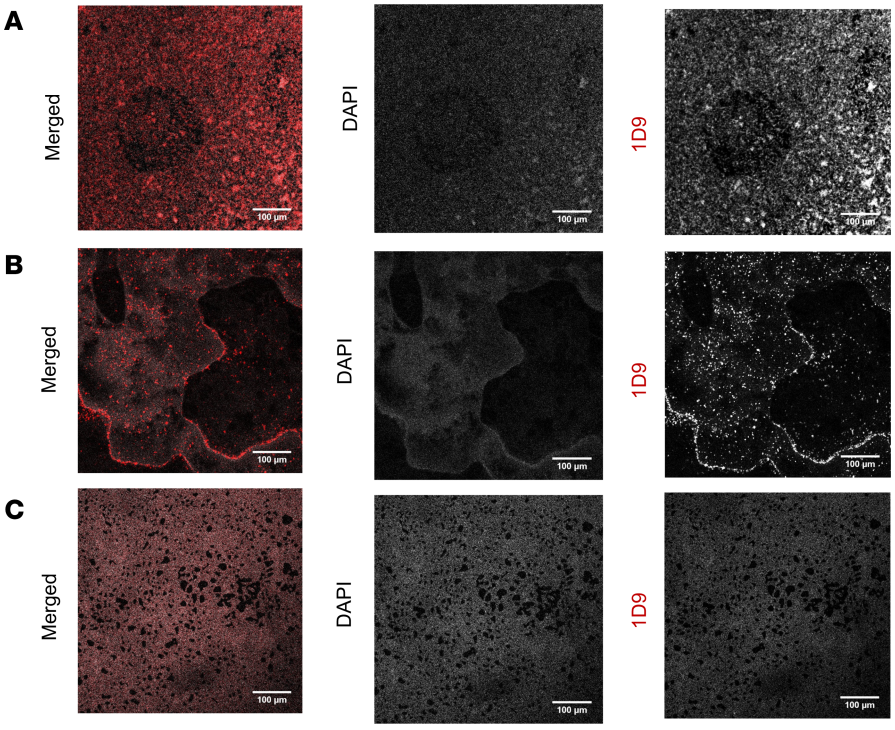

Figure 1. In vitro detection of *S. aureus* IsaA in biofilms using 1D9–Alexa Fluor 555. Biofilms of (**A**) *S. aureus* Xen36, (**B**) *S. aureus* SH1000, and (**C**) *S. aureus* MS001 (Δ*isaA*) were grown on coverslips for microscopy and, subsequently, stained with DAPI and the IsaA-specific monoclonal antibody 1D9 labeled with Alexa Fluor 555. Images recorded by confocal microscopy show the *S. aureus* DNA staining with DAPI (gray), IsaA staining with 1D9–Alexa Fluor 555 (red), and a merged image. Scale bars: 100 µm. Note that *S. aureus* MS001 (Δ*isaA*) shows some residual binding of 1D9–Alexa Fluor 555 due to the presence of the IgG-binding proteins Spa and Sbi (26).

mentioned that the spinal implant *S. aureus* infection also resulted in increased systemic inflammation with an elevated SUV signal in the spleen. On POD 42, *S. aureus* CFUs were enumerated from ex vivo implants and tissue, and CFUs were only detected from implants of infected mice but not sterile mice (Figure 4, J and K), confirming the in vivo BLI data, as previously described for this model (Figure 4I) (27, 28).

^{89}Zr-NIR680-1D9 PET-CT imaging. The 1D9 antibody was dual labeled with ^{89}Zr and NIR680 (^{89}Zr-NIR680-1D9) to assess specificity for *S. aureus* with PET-CT and FLI in the mouse model of *S. aureus* spinal implant infection (Figure 5). ^{89}Zr enabled assessment of probe viability over a longer time frame than ^{18}F-FDG due to its longer half-life. On POD 8, ^{89}Zr-NIR680-1D9 was administered, and accumulation of the probe was assessed by PET-CT imaging on POD 11 (Figure 5). Increased ^{89}Zr-NIR680-1D9 accumulation was observed in infected versus sterile mice (SUV_{mean} 2.96 ± 0.22 vs. 2.01 ± 0.18; $P < 0.001$) (Figure 5I). The probe remained at the site of *S. aureus* infection for at least 7 days (POD 18), indicating longitudinal probe stability (Figure 5G). On POD 18, the difference between infected and sterile mice increased further due to a lack of change in the SUV_{mean} in infected mice, but there was a decrease in the SUV_{mean} in sterile mice (SUV_{mean} 3.01 ± 0.23 vs. 1.54 ± 0.44; $P < 0.001$) (Figure 5J).

^{89}Zr-NIR680-1D9 FLI. As an additional method to noninvasively detect the *S. aureus* spinal implant infection, after administration of ^{89}Zr-NIR680-1D9 on POD 8, FLI was performed on POD 11 and POD 18 (Figure 5, E–H). Similar to results with PET-CT imaging, the FLI signal was significantly higher in infected mice than in sterile mice ($2.72 \times 10^9 \pm 1.19 \times 10^9$ vs. $6.60 \times 10^8 \pm 3.56 \times 10^8$ total radiant efficiency; $P < 0.01$) (Figure 5K). However, on POD 18 both absolute FLI signals and differences between infected and sterile mice decreased substantially and were no longer statistically different, suggesting that the fluorescent dye attached to 1D9 was either less stable or less sensitive than ^{89}Zr PET/CT imaging (Figure 5L).

FLI-guided surgical debridement. An intraoperative experiment was performed to assess whether *S. aureus* labeled with ^{89}Zr-NIR680-1D9 could be visualized and debrided in real-time using FLI-guided surgery. FLI-guided surgical debridement of infected tissue was performed in real time on POD 10 after spinal implant surgery using the Solaris Fluorescence Image-Guided Surgery System (PerkinElmer) (Figure 6).

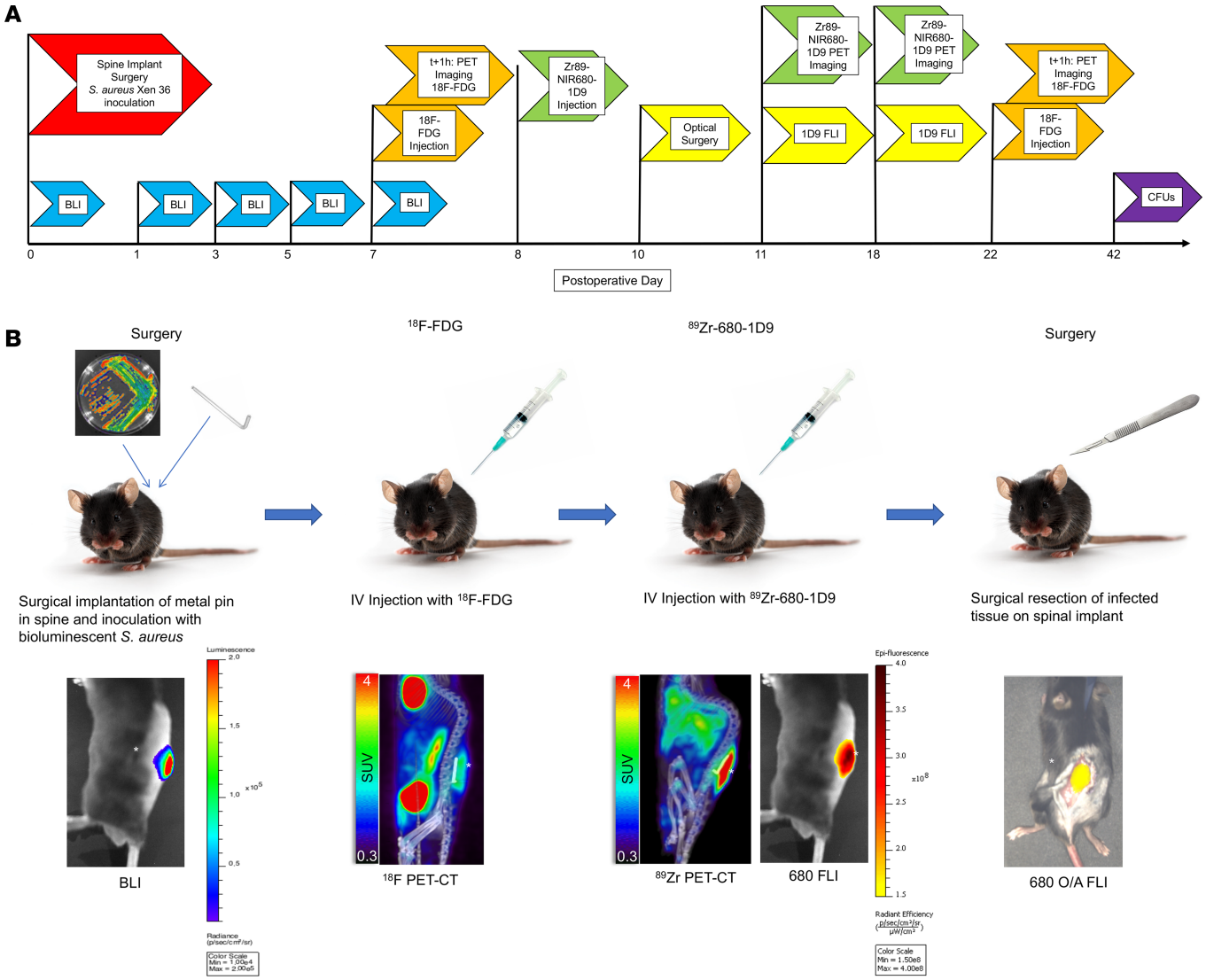

Figure 2. Experimental timeline and overview. (**A**) Timeline. Full details are provided in the Methods. Procedures performed on mice on given postoperative days are indicated with flags. BLI, bioluminescence imaging; FLI, fluorescence imaging; 18F-FDG, fluorodeoxyglucose; 1D9, *Staphylococcus* antibody probe; Zr89-NIR680-1D9, 89-zirconium–labeled *Staphylococcus* antibody probe; CFUs, enumeration of CFUs; optical surgery, surgical debridement via the Solaris instrument. (**B**) Experimental overview. Zr89-680-1D9, dual 89-zirconium NIR680-labeled *Staphylococcus* antibody probe; SUV, standard uptake value; O/A FLI, optical-assisted (fluorescent) surgical debridement. The asterisks indicate the location of infection (neighboring color density).

Partial excision of infected tissue was performed, and confirmation of the *S. aureus* infection was performed by identifying FLI signal from both the excised tissue as well as remaining infected tissue at the surgical site. The surgeon confirmed that the FLI signal was superimposed over the visually evident inflammatory tissue around the infected spinal implant.

Discussion

The present study addresses the current clinical need for accurate, noninvasive diagnosis of surgical implant infection. When evaluating a patient with potential implant infection, the surgeon is limited by three key factors. First, it is impossible to confidently discriminate infection from aseptic loosening due to limitations in current imaging modalities, including metal artifacts from the implant (15–22). Second, the surgeon cannot differentiate *S. aureus* from other bacteria, a distinction that affects management and prognosis; species-specific intraoperative antimicrobial adjuvants can only be utilized if the bacteria is diagnosed prior to completing the operation (9, 11, 12). Third, the surgeon must intraoperatively rely solely on visual inspection of affected tissue, which makes an assessment of the extent of disease imprecise.

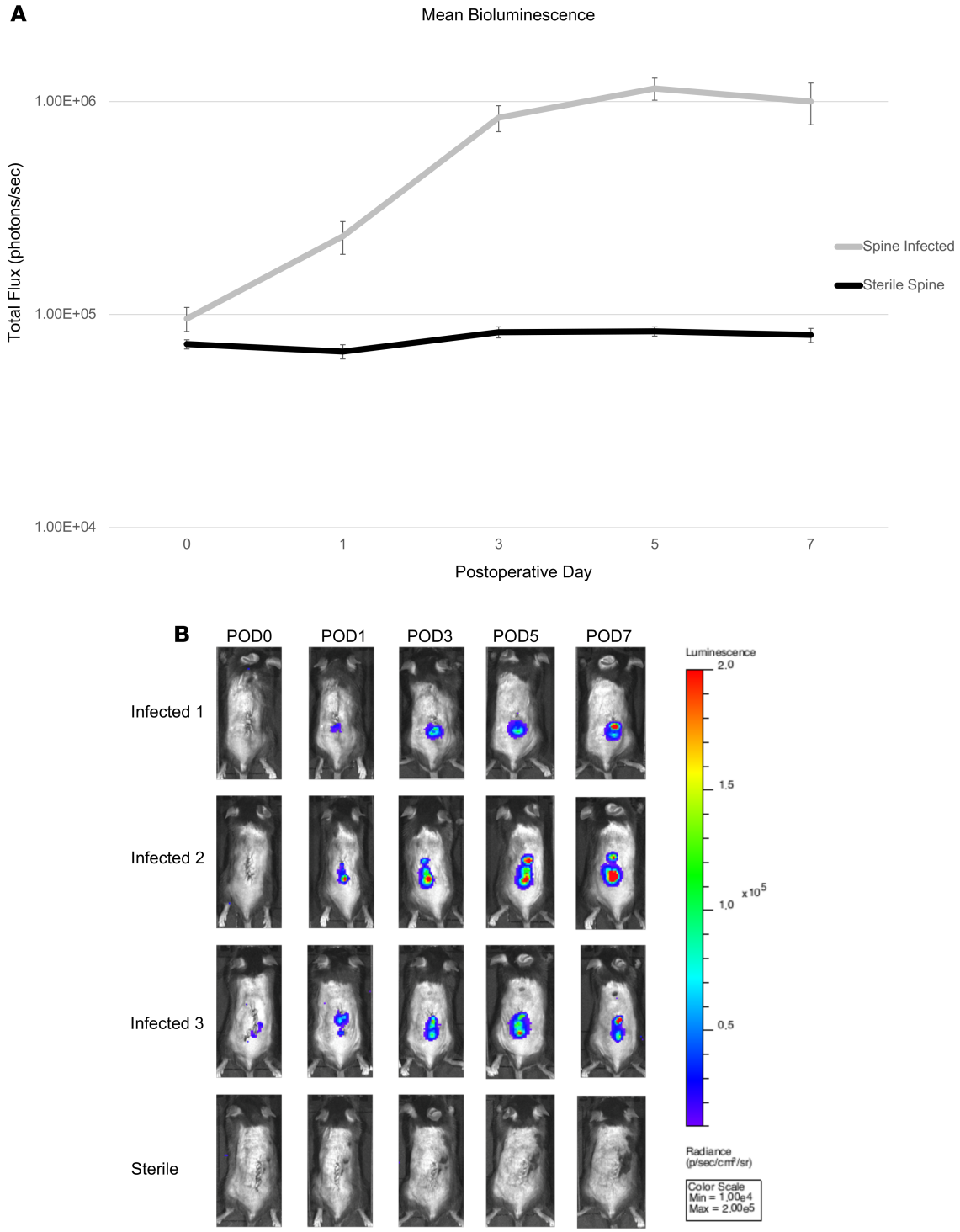

Figure 3. Bioluminescence imaging. (**A**) Bioluminescence (BLI) in infected (n = 11) and sterile (n = 4) mice. Mean total BLI, represented as total flux (photons/s) at each postoperative time point. Error bars represent SEM. (**B**) Representative BLI images from 3 infected and 1 sterile mouse at postoperative time points.

To address this problem, we verified the feasibility of sensitive, noninvasive, and real-time diagnosis of *S. aureus* implant infection in an established mouse model of spine implant infection. This was accomplished by using the ^{89}Zr-NIR680-1D9 dual-labeled antibody probe with multimodal PET-CT and in vivo FLI. These data provide the proof of concept for a noninvasive approach to diagnose a specific pathogen preoperatively, guide surgical debridement intraoperatively, and evaluate treatment effectiveness postoperatively in a challenging patient population with spinal implants.

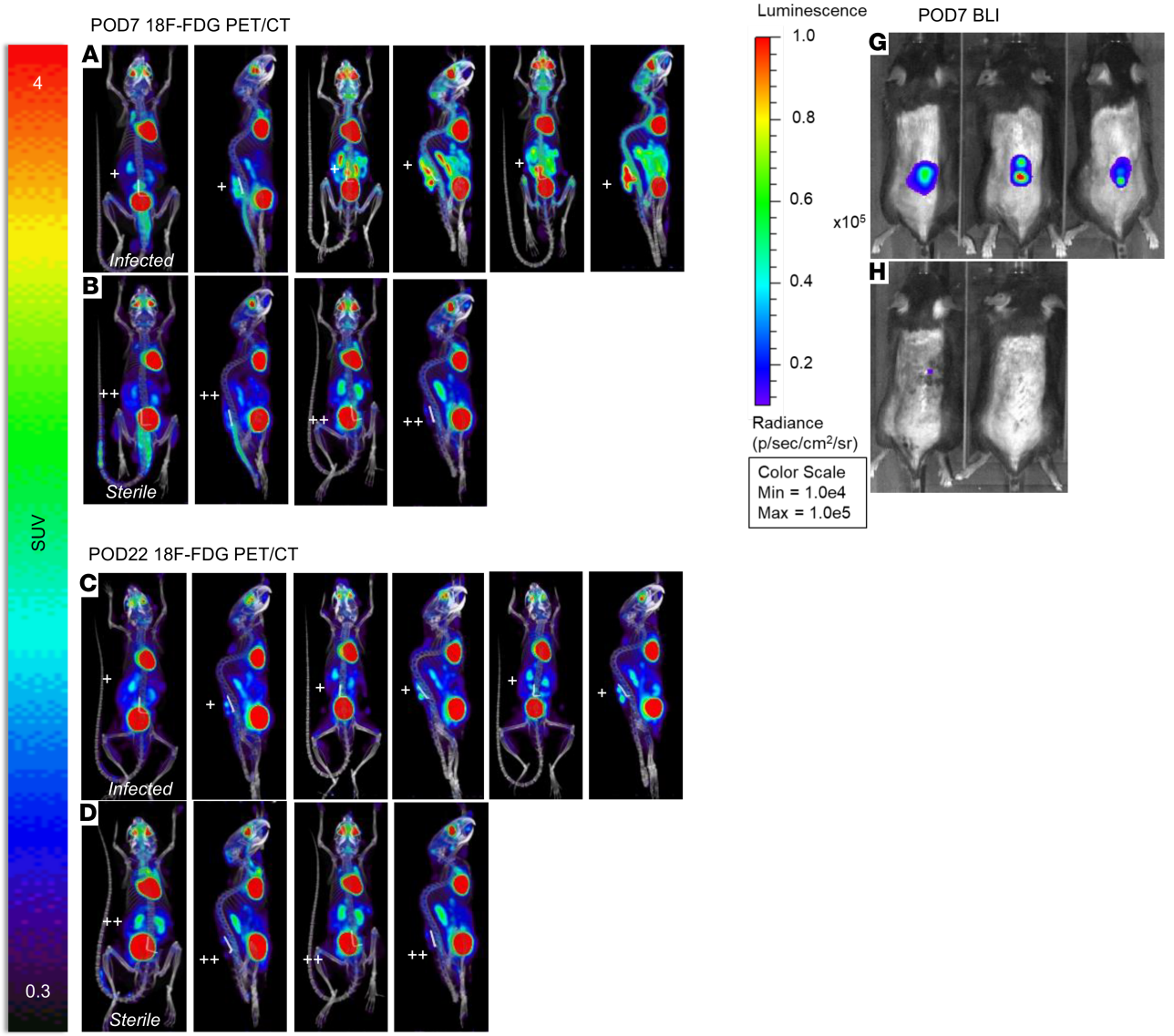
POD7 18F-FDG PET/CT
A
Infected
B
Sterile
SUV
4
0.3
POD22 18F-FDG PET/CT
C
Infected
D
Sterile
Luminescence
1.0
0.8
0.6
0.4
0.2
x10^5
Radiance (p/sec/cm²/sr)
Color Scale
Min = 1.0e4
Max = 1.0e5
POD7 BLI
G
H

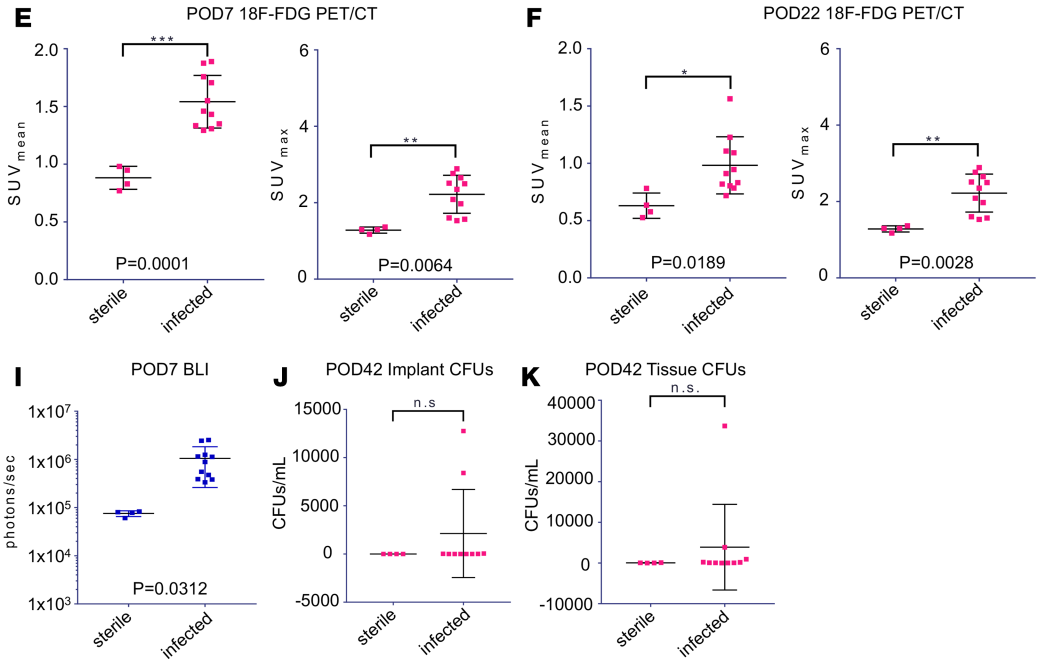
E
POD7 18F-FDG PET/CT
SUV mean
SUV max
P=0.0001
P=0.0064
F
POD22 18F-FDG PET/CT
P=0.0189
P=0.0028
sterile
infected

I
POD7 BLI
photons/sec
P=0.0312
J
POD42 Implant CFUs
CFUs/mL
n.s
K
POD42 Tissue CFUs
n.s.
sterile
infected

Figure 4. ^{18}F-FDG PET imaging. ^{18}F-FDG PET/CT imaging was performed on POD 7 (acute infection) and POD 22 (chronic infection) in (n = 11) infected mice and (n = 4) sterile mice (see Methods and Figure 1). PET images were performed on the G8 PET/CT imaging system (PerkinElmer). (**A**) Selected coronal and sagittal PET images of 3 infected mice on POD 7. (**B**) Selected coronal and sagittal PET images of 3 sterile mice on POD 7. (**C**) Selected coronal and sagittal PET images of 3 infected mice on POD 22. (**D**) Selected coronal and sagittal PET images of 3 sterile mice on POD 22. (**E**) SUV_{mean} and SUV_{max} for infected and sterile mice on POD 7. (**F**) SUV_{mean} and SUV_{max} for infected and sterile mice on POD 22. (**G**) Bioluminescence images of infected mice on POD 7. (**H**) Bioluminescence images of sterile mice on POD 7 (**I**) BLI data for infected and sterile mice on POD 7. (**J**) CFUs cultured from the implant on POD 42 after implant infection inoculation. (**K**) CFUs cultured from surrounding tissue on POD 42 after implant infection inoculation. CFUs were analyzed in (n = 10) infected mice and (n = 4) sterile mice. +, infected steel implant; ++, sterile steel implant; BLI, bioluminescence imaging; SUV, standard uptake value. Cross bars represent the mean. Error bars represent SEM. The statistical test used was 2-tailed Student's t test; $^{*}P \le 0.05$, $^{**}P \le 0.01$, $^{***}P = 0.0001$.

Prior studies have reported *S. aureus*–specific imaging probes using labeled antibiotics (29), peptides (30–32), bacteriophage (33), carbon nanotubes (33), and clotting factors (34). While promising, most continue to be limited by suboptimal specificity and clinical applicability (35). Our group therefore recently developed and validated the specificity of the 1D9 antibody, which was able to accurately distinguish a *S. aureus* infection from other bacteria or sterile inflammation (26). The specificity of this particular probe is encouraging and prompted the current study. However, our findings indicate that the probe has the capability to detect clinically relevant biofilm-associated infection that it is far superior over conventional ^{18}F-FDG PET-CT imaging (20, 22, 36–41) and that it provides the opportunity for FLI-guided intraoperative surgical debridement. In addition, the multimodal capability of ^{89}Zr-NIR680-1D9 permits increased sensitivity and specificity via PET-CT, which is not affected by tissue quality or presence of metal artifact (42). Further, PET is clinically relevant, as there is established availability and clinical use of PET-CT imaging equipment throughout the United States and worldwide; the existence of FDA approvals and clinical use of the relevant radiolabeled tracers (^{18}F-FDG and ^{89}Zr) permits incorporation into practice (43, 44), and the feasibility of open-air optical imaging has been previously demonstrated in surgical fields (45, 46).

This study has several limitations. First, ^{89}Zr was chosen for its long half-life (72.4 hours), enabling us to assess the stability of the 1D9 component over a longer time period (11 days, versus only a few hours with ^{18}F-FDG). However, ^{89}Zr has the potential for release of Zr^{4+} from conjugation with deposition into bone marrow, which could be prevented with advances in chelator technology, such as DFO used in the present study (44). Second, the FLI signals could have been influenced by factors, such as body habitus, hair regrowth, and skin pigmentation, which might have contributed to decreased sensitivity of in vivo FLI compared with ^{89}Zr/PET-CT imaging. This has important implications for translation, as optimal timing of probe injection prior to surgical debridement would need to be established. Finally, as a preclinical study in a mouse model, there are obvious differences from humans in the complexity of surgery, extent of infection burden, and depth of tissue. However, we believe the advantages of using this mouse model as a proof of concept outweigh its limitations: the ease of reproducibility and relative cost-effectiveness compared with large-animal studies permit a well-powered study, and the ability to genetically modify the host permits future adaptive studies. Additionally, the longitudinal nature of the bioluminescent imaging permits rapid accumulation of data while minimizing animal burden and, at the same time, promoting confirmation of infection intensity.

In conclusion, in this preclinical spinal implant *S. aureus* infection model, the ^{89}Zr-NIR680-1D9 dual-labeled probe in conjunction with PET-CT and FLI imaging provided the capability for preoperative, noninvasive, and specific diagnosis of an *S. aureus* spinal implant infection and for intraoperative surgical debridement. We are hopeful that our data represent a promising target imminently available to clinicians, permitting the distinction of infection from aseptic loosening, differentiation of *S. aureus* from other pathogenic bacteria, and FLI-guided surgical debridement. Further, as antibodies are readily designed against a host of bacteria species, this work opens up the possibility of widespread applications against a multitude of infectious targets. As infection is a major complication for many implants, devices, and prostheses, in addition to spinal implants (9), our results might have broad clinically applicability to improve the diagnosis and treatment of biofilm-associated infections.

Methods

S. aureus bioluminescent strain. The bioluminescent *S. aureus* strain Xen36 (PerkinElmer) was used as the inoculum of interest. This strain was derived from the parental strain *S. aureus* ATCC-49525 (Wright), which is a clinical isolate from a septic patient. This specific bioluminescent derivative has been utilized in

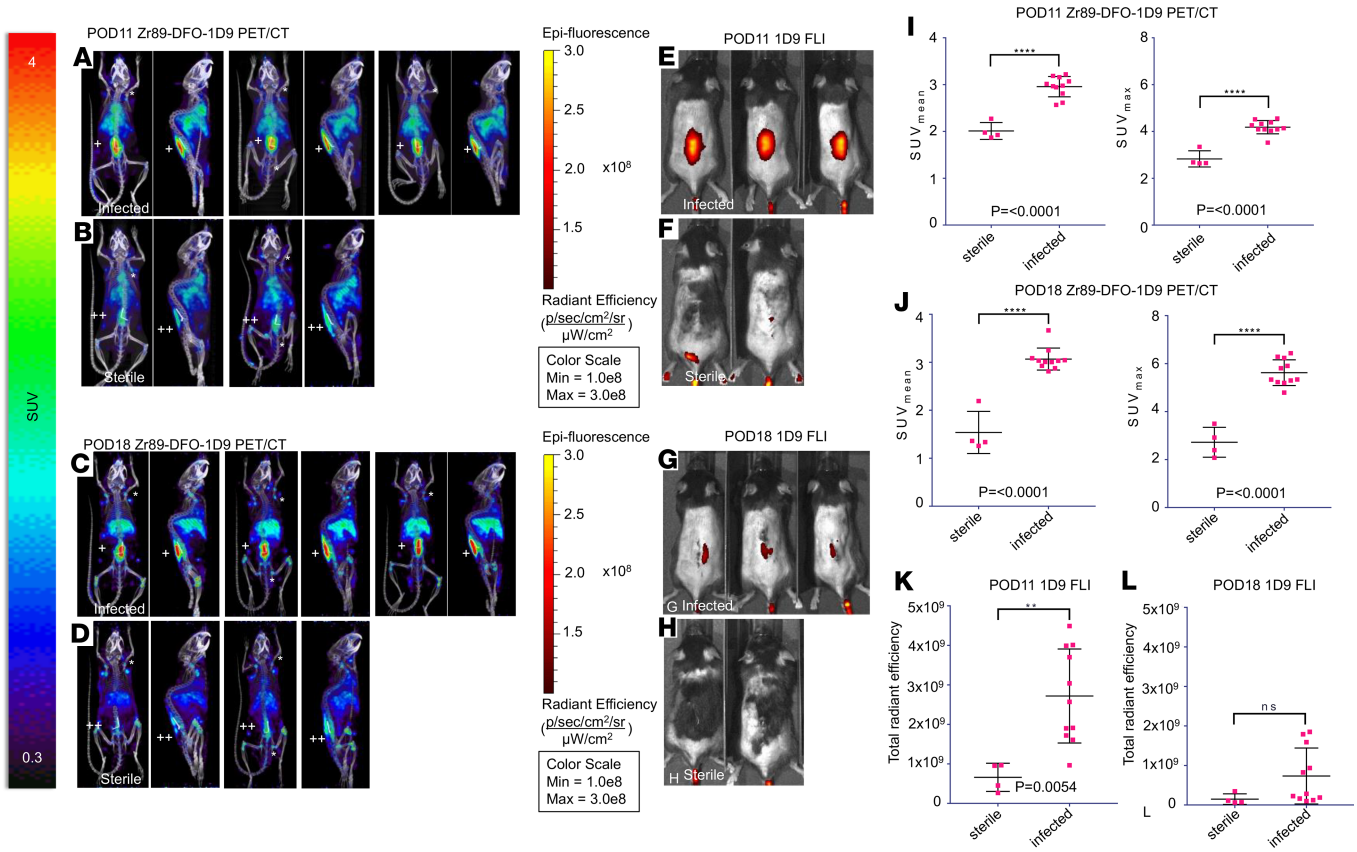

Figure 5. ^{89}Zr-680-1D9 PET Imaging. ^{89}Zr-680-1D9 PET/CT imaging was performed on POD 11 (acute infection) and POD 18 (chronic infection) in (n = 11) infected mice and (n = 4) sterile mice (Figure 1B). Fluorescence labeled antibody targeting *S. aureus* (NIR680-1D9) was radiolabeled with ^{89}Zr for PET imaging, and antibody probe was also imaged separately on FLI (see Methods). (**A**) Selected coronal and sagittal PET images of 3 infected mice on POD 11. (**B**) Selected coronal and sagittal PET images of 3 sterile mice on POD 11. (**C**) Selected coronal and sagittal PET images of 3 infected mice on POD 18. (**D**) Selected coronal and sagittal PET images of 3 sterile mice on POD 18. (**E**) Fluorescence images of infected mice on POD 11. (**F**) Fluorescence images of sterile mice on POD 11. (**G**) Fluorescence images of infected mice on POD 18. (**H**) Fluorescence images of sterile mice on POD 18. (**I**) SUV_{mean} and SUV_{max} for infected and sterile mice on POD 11. (**J**) SUV_{mean} and SUV_{max} for infected and sterile mice on POD 18. (**K**) FLI data for infected and sterile mice on POD 11. (**L**) FLI data for infected and sterile mice on POD 18. +, infected steel implant; ++, sterile steel implant; FLI, fluorescence imaging; SUV, standard uptake value. The asterisks indicate axillary, brachial, and inguinal lymph nodes. Error bars represent SEM. The statistical test used was 2-tailed Student's t test; $^{**}P \le 0.01$, $^{****}P < 0.0001$.

prior validated studies (27, 47). *S. aureus* Xen36 uniquely utilizes a *lux*ABCDE operon, which is optimized and integrated into the host's native plasmid (48). As a result, the Xen36 strain is capable of producing a blue-green bioluminescent light with a peak wavelength emission of 490 nm. This emission signal is only produced by living metabolically active bacterial organisms. Previous research has shown that the Xen36 strain is therefore optimal for research focusing on the longitudinal monitoring of bacterial burden through bioluminescence (Supplemental Figure 4) (47).

1D9 antibody. 1D9 is a fully human IgG1 monoclonal antibody specific for the *S. aureus* IsaA protein (25, 26, 49). In-house production and purification of 1D9 was performed as described by Romero Pastrana et al. (25, 26). Briefly, 1D9 was produced by transient transfection of Expi293F cells (Life Technologies). 1D9 antibodies were then purified from the cell culture medium using a HiTrap Protein A HP column (GE Life Sciences) and subsequent HiTrap column desalting (GE Life Sciences).

In vitro S. aureus biofilm detection with 1D9 fluorescent probe. *S. aureus* strains Xen36, SH1000 (50), and MS001 (Δ*isaA*) (51) were grown overnight in tryptic soy broth (TSB) in a shaking incubator at 37°C. *S. aureus* biofilms were grown on 13-mm coverslips in a 24-well plate containing TSB, supplemented with 5% glucose and 3% NaCl, and inoculated with the overnight culture to an optical density at 600 nm (OD600) of 0.1. The Alexa Fluor 555 dye (Thermo Fisher Scientific) was cross-linked to the human monoclonal antibody 1D9 via activated N-hydroxysuccinimide ester chemistry. Coverslips with biofilm were incubated with 30 μg/ml of the 1D9–Alexa Fluor 555 conjugate for 30 minutes in PBS. To remove unbound antibody,

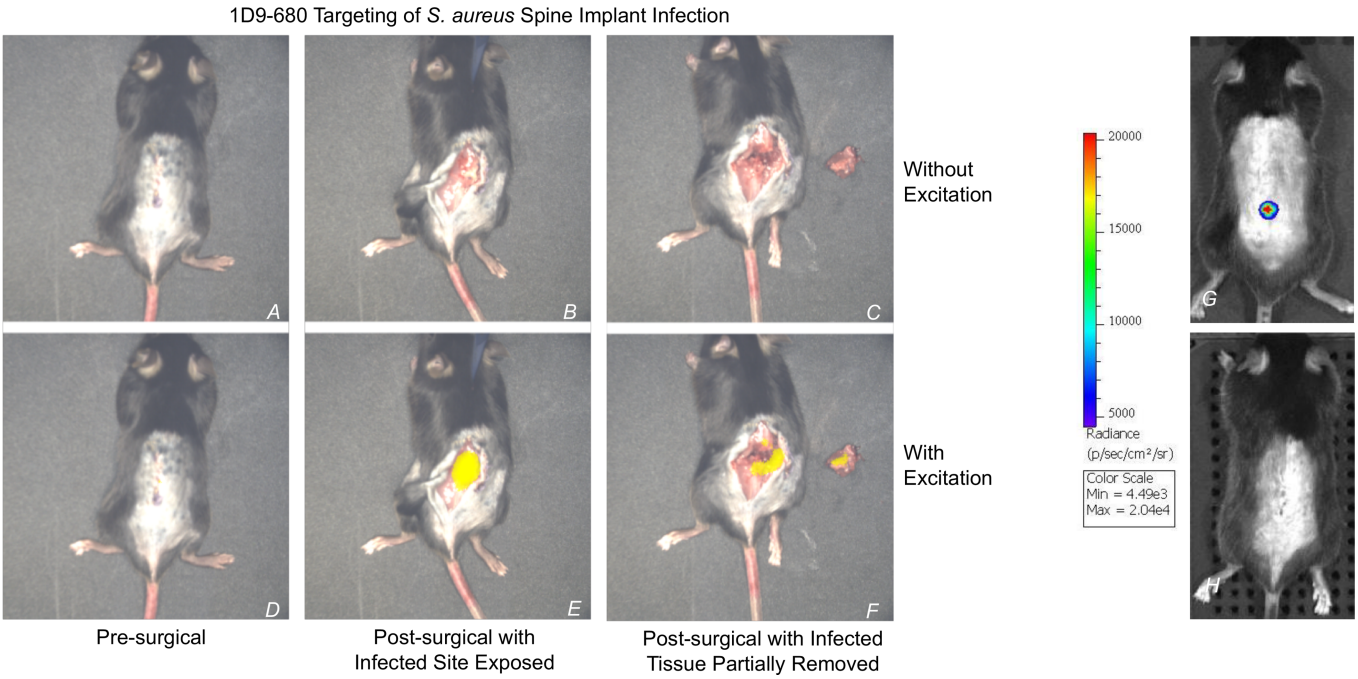

Figure 6. NIR680-1D9 targeting of *S. aureus* spine implant infection. Following identification of infection with ^{18}F-FDG and ^{89}Zr-680-1D9 PET imaging, infection was then visualized using the Solaris Fluorescence Image-Guided Surgery System (PerkinElmer). On POD 10, 48 hours after 1D9 antibody probe i.v. injection on POD 8, a mouse with acute spinal implant infection was isolated under the image-guided surgery system and analyzed both with and without fluorescent excitation at 680 nm. Prior to skin incision (**A** and **D**), no fluorescent signal was visible. Following skin incision (**B** and **E**), fluorescent signal was only present with excitation. Following partial excision of infected tissue, as identified by fluorescent signal (**C** and **F**), fluorescent signal remained present both in host tissue and explanted tissue. (**G**) BLI of the infected mouse on POD 7. (**H**) BLI of a sterile mouse on POD 7. BLI, bioluminescence imaging; ^{89}Zr, 89-zirconium; 1D9, *Staphylococcus* antibody probe.

the biofilms were washed with 1× PBS and, thereafter, fixed in 4% paraformaldehyde in 1× PBS. Finally, the DNA of the bacteria was stained with DAPI (Roche), and the coverslips were mounted on microscopy slides. Image acquisition was performed with a Leica TCS SP8 confocal microscope. The recorded images were processed using ImageJ software (National Institutes of Health).

Preparation of S. aureus for inoculation. Bacterial preparations were performed in accordance with previously published experiments, with minor alterations as needed (27, 47). First, *S. aureus* Xen36 was isolated from potential contaminants using kanamycin plates. This is possible due to a kanamycin resistance gene linked to its aforementioned *lux* operon (48). As such, 200 μg/ml kanamycin (MilliporeSigma) was added to ensure purity. *S. aureus* Xen36 was then streaked onto agar plates (Luria Broth plus 1.5% bacto agar, Teknova) and cultured at 37°C for approximately 24 hours. Single colonies of *S. aureus* Xen36 were then isolated and individually grown in TSB and cultured again for 24 hours at 37°C in a shaking incubator (200 rpm) (MaxQ 4,450, Thermo). After an additional 2 hour subculture of a 1:50 dilution from the resultant culture, midlogarithmic phase bacteria were isolated. Finally, after centrifugation, bacterial cells were pelleted, resuspended, and washed in PBS. A single bacterial inoculum (1×10^3 CFUs in 2 μl PBS) was approximated by measuring the absorbance at 600 nm (A600, Biomate 3, Thermo Fisher). This dose was determined based on a previously published protocol (27).

Mice. Twenty-four 12-week-old male C57BL/6J wild-type mice (JAX 000664, Jackson Laboratories) were utilized for experimental purposes. According to institutional ARC protocol, all mice were housed in cages, a maximum of 4 at a time, and stored with a 12-hour light/dark cycle. During the dark phase of the cycle, no experimentation was permitted. Water was available at all times. Due to potential interference with FLI signaling, alfalfa-free chow was used for feeding. Veterinary staff assessed mice daily to ensure the well-being of the animals throughout the entirety of the experiment. The transportation of mice to PerkinElmer facilities in Hopkinton, Massachusetts, USA, on POD 5 was conducted in accordance with institutional ARC protocol.

Mouse surgical procedures. Surgical implantation of spinal implant was performed in accordance with previously published protocols (27). In brief, mice were anesthetized in the prone position by utilizing inhaled

isoflurane (2%) via nose cone on a sterile surgical bed. Hair was removed from sacrum to upper thoracic spine with rodent clippers. Skin was cleansed and sterilized with triple washes of alternating Betadine solution and isopropyl alcohol. Knees were maximally flexed to identify approximate level of L4 vertebral body. A longitudinal 2-cm incision was made through skin with a 15-blade surgical scalpel. The spinous processes were palpated in midline, and the incision was carried down to bone. Subperiosteal dissection was performed on the right side of the spinous process, carried lateral to the transverse process, at the level of the L4 vertebral body. Absorbable braided suture size 5-0 was passed cephalad and caudad to the L4 body through the fascia and left open, in preparation for future closure. A 25-gauge spinal needle was used to ream the spinous process of L4, followed by implantation of a 0.1-mm "L-shaped" surgical grade stainless steel implant (Modern Grinding), and was laid down along the lamina with the long arm laying cephalad. The implant was inoculated with 1×10^3 CFUs/2 μl bioluminescent *S. aureus* Xen36, taking care to ensure all solution contacted the implant. The previously passed absorbable suture was tied immediately following inoculation to ensure containment of inoculum on the implant. The skin was closed in running fashion with absorbable suture. Pain medicine was administered via subcutaneous injection of subcutaneous buprenorphine (0.1 mg/kg) (Zoopharm) immediately postop and then every 12 hours for 3 days thereafter. Mice recovered on a heating pad and monitored for the appropriate return to normal activity. Postoperative radiographs (Faxitron LX-60 DC-12 imaging system) confirmed appropriate placement of implant.

Confirmation of S. aureus infection with BLI. Mice were anesthetized by utilizing inhaled isoflurane (2%). Once anesthetized, in vivo BLI was performed using the IVIS Lumina II (PerkinElmer) (48). Imaging was performed in accordance to previously published protocols (27). Bacterial burden was confirmed on POD 0, 1, 3, 5, and 7 (Figure 2). Data are presented via color scale overlaid on a grayscale photograph and were quantified as total flux (photons per second) within a standard ovoid region of interest (ROI) (~16,000 pixels) using LivingImage Software (PerkinElmer) (Figure 3). These intensities were averaged with respect to the SEM (Figure 3A).

^{18}F-FDG PET injection, 1D9 injection, and imaging. We first performed a validation experiment with ^{18}F-FDG microPET imaging using the G8 PET-CT system (PerkinElmer) to detect active glucose uptake associated with microbial infection and tissue inflammation (Supplemental Figures 2 and 3). Each mouse received 100 μCi ^{18}F-FDG (PETNET Solutions Inc.) via i.v. injection. The animals were kept warm and maintained under 1.5% isoflurane gas anesthesia for 1 hour for tracer uptake. Subsequently, the mice were imaged with a standard 10-minute static ^{18}F-PET imaging protocol followed by a standard 2-minute whole-body CT scan. After acquisition, the imaging system automatically produced reconstructed 3D tomography images in the DICOM format. We used the VivoQuant 3.0 software (inviCRO Inc.) for PET/CT data viewing and SUV_{max} analysis.

For validating NIR680-1D9 experiments, each mouse received 0.100 μg NIR680-1D9 antibody in 40 μl DMSO via tail vein injection. Three mice with confirmed implant infections on POD 7 and two sterile mice were each injected; 48–72 hours after injection, FLI was performed using the IVIS Lumina II imaging system (PerkinElmer) to detect fluorescence (excitation: 640 nm, emission: 695–770 nm). We used the Living Image Software (PerkinElmer) for data viewing and analysis.

Bioluminescence and ^{18}F-FDG PET/CT imaging. Following completion of the validation experiments, a subsequent experiment was performed (Figure 4). On POD 7 and POD 22 after infection of *S. aureus*, 11 infected and 4 sterile control mice underwent bioluminescence and ^{18}F-FDG PET-CT imaging. Mice were anesthetized with 1.5% isoflurane, placed in a sterile imaging chamber, and imaged using the IVIS Lumina II imaging system (PerkinElmer) to detect bioluminescence. Subsequently, mice were injected i.v. via lateral tail vein with approximately 75 μCi ^{18}F-FDG and underwent 60 minutes of uptake under 1.5% isoflurane anesthesia and heating. This was followed by PET and CT imaging on the G8 PET-CT (PerkinElmer), an integrated scanner with a PET subsection that consists of 8 detector blocks, each with a 24 × 26 BGO scintillator array and crystals measuring 1.825 × 1.825 × 7 mm arranged in a box geometry and a back section consisting of a rotating CT gantry. PET images were acquired for 600 seconds with an energy window of 150–650 keV, reconstructed using maximum-likelihood expectation maximization, as recommended by the vendor. PET images were corrected for CT-based photon attenuation, detector normalization, and radioisotope decay (scatter correction was not applied) and converted to SUVs. PET-CT images were analyzed by drawing ROIs over the implant region using AMIDE version 1.0.5 imaging software (52). Bioluminescence images were similarly analyzed using LivingImage version 4.5.

1D9 DFO conjugation and ^{89}Zr-radiolabeling. The human monoclonal antibody 1D9 was fluorescently labeled with NIR680 (PerkinElmer) to yield NIR680-1D9 as previously described (25). NIR680-1D9 was conjugated to desferrioxamine (DFO) using a modified previously published procedure (53). A 5-fold molar excess of the p-isothiocyanatobenzyl-derivative of DFO (p-SCN-Bn-DFO; B-705, Macrocyclics) dissolved in DMSO at a 5 mM concentration was incubated with 3.6 mg NIR680-1D9 in 0.1 M borate buffer, pH 8.0, at 35°C for 4 hours (54). Unbound p-SCN-Bn-DFO was removed by size-exclusion chromatography using a PD-10 column and PBS as eluent. Eluted DFO-1D9 was concentrated to 6.6 mg/ml using an Amicon Ultra-4 centrifugal filter device (Millipore) and sterile filtered through a 0.22-μm PVDF syringe filter.

The DFO-1D9 was radiolabeled with ^{89}Zr (3D Imaging). ^{89}Zr in 1 M oxalic acid (4.1 mCi in 15 μl) was adjusted to pH 7.0 by the addition of 2 M sodium carbonate (6 μl) and 1 M HEPES buffer, pH 7.0 (37.5 μl), in a 1.6-ml microcentrifuge tube; this was confirmed by a pH paper test strip. The solution was diluted with an additional 30 μl deionized water. 2.5 mCi (67 μl) neutralized ^{89}Zr was incubated with 519 μg DFO-1D9 for 60 minutes at room temperature to form ^{89}Zr-DFO-1D9. Following incubation, the percentage of radioactivity bound to DFO-1D9 was determined to be 99.8% using instant thin-layer chromatography strips (Biodex Medical Systems) and 20 mM citrate buffer, pH 5.0, as the running buffer.

PET-CT and FLI of 1D9. On POD 7, after infection of *S. aureus* and after bioluminescence and ^{18}F-FDG PET-CT imaging, the same 11 infected and 4 sterile control mice were injected i.v. via the lateral tail vein with 68.6 ± 1.6 μCi (~14 μg) of ^{89}Zr-680-1D9 mAb (specific activity 4.89 μCi/μg). Mice underwent PET-CT imaging on the G8 and fluorescence (excitation: 640 nm, emission: 695–770 nm) imaging on the IVIS Lumina II on day 3 and 10 after ^{89}Zr-680-1D9 injection, as described above (Figure 2). The relative concentrations of ^{89}Zr-680-1D9 in the spine implant region by PET and FLI were determined by drawing ROIs using AMIDE and LivingImage imaging software, respectively.

Bacterial colony enumeration. In order to validate the bioluminescence signal of bacterial burden, bacteria adherent to the spinal implants were quantified at the conclusion of the experiment (POD 42) via subject euthanasia. Bacteria were then removed from the implant by sonication in 500 μl of 0.3% Tween-80 in TSB for 15 minutes, followed by vortex for 2 minutes based on a previously validated protocol (27). Simultaneously, bacteria in the surrounding tissue were measured by homogenizing the surrounding muscle and vertebral bodies (Pro200H Series homogenizer; Pro Scientific). The number of bacterial CFUs that were adherent to the implant and in the surrounding tissue was determined by counting individual colonies after 24-hour culture. Units were expressed as CFU/ml. After CFU harvest, colonies were imaged using the IVIS Lumina for bioluminescence, confirming the presence of *S. aureus* Xen36.

Optical guided debridement with Solaris. In order to demonstrate the clinical translatability of the theragnostic model we developed, we subjected a sample mouse to the Solaris Fluorescence Image Guided Surgery System (PerkinElmer) (Figure 6). The mouse was positioned prone in the standard operative manner and was subjected to general anesthesia with 2.5% inhaled isoflurane. The Solaris system was then used on the 660 channel, with excitation/emission parameters of 667/692–742 nm. The mouse was imaged both with and without excitation. A partial surgical debridement of fluorescently tagged subcutaneous tissue was performed using an 11-blade scalpel and surgical forceps.

Statistics. Eleven mice were in the infection cohort and four mice were in the sterile control cohort. Two-tailed Student's *t* test was used to compared data between the groups. *t* values (5.249, 8.911, 3.244, and 3.670) were calculated at early and late time points for ^{89}Zr and ^{18}F-FDG, respectively. The degree of freedom was 13. Data collection was performed by two independent reviewers at all time points. Data are represented as mean ± SEM. $P < 0.05$ was considered statistically significant. Statistical analyses were performed using Stata Statistical Software (StataCorp., release 14).

Study approval. All test subjects were obtained and utilized with good animal practice as mandated by federal regulations in accordance with the Animal Welfare Act, the *Guide for the Care and Use of Laboratory Animals* (National Academies Press, 1996), the Public Health Service Policy for the Humane Care and Use of Laboratory Animals, and the policies and procedures set forth in the UCLA Animal Care and Use Training Manual. In addition, all animal research was approved and regulated by the UCLA Chancellor's Animal Research Committee (ARC 2012-104-03J).

Author contributions

SDZ developed hypotheses, designed experiments, collected data, analyzed results, created figures, drafted the manuscript, and performed critical revisions of the manuscript. HYP performed mouse surgeries, analyzed results, and performed critical revisions of the manuscript. TO and CZ performed PET-CT imaging and drafted sections of the manuscript. ZDB and GB analyzed results and performed critical revisions of the manuscript. WLS, CDH, and KRH assisted in mouse surgeries, collected data, and analyzed data. JCT, JC, and CM collected data and performed PET imaging. JTL managed PET imaging and drafted critical sections of the manuscript. EJMR performed biofilm experiments and confocal microscopy. FRP produced and purified critical experimental material. MB performed biofilm experiments and microscopy. JFM, LSM, and JMVD provided intellectual ideas and support and performed critical revisions of the manuscript. KPF provided intellectual ideas and support, coordinated team members, and performed critical revisions of the manuscript. NMB provided funding, intellectual ideas, and support and performed critical revisions of the manuscript.

Acknowledgments

Research reported in this publication was supported by the National Institute of Arthritis and Musculoskeletal and Skin Diseases of the National Institutes of Health under Ruth L. Kirschstein National Research Service Award T32AR059033 and Award 5K08AR069112-01. The content is solely the responsibility of the authors and does not necessarily represent the official views of the National Institutes of Health. FRP received a scholarship from the National Council for Science and Technology (CONACyT, 169643). EJMR received funding from the Commission of the European Union (CEU) Marie Skłodowska-Curie Innovative Training Network (MSCI-ITN) grant 713482 (ALERT). MB received funding from CEU MSCI-ITN grant 713660 (Pronkjewail). Part of this work was performed at the University Medical Center Groningen Imaging and Microscopy Center, which is sponsored by grants from the Netherlands Organisation for Scientific Research (40-00506-98-9021, TissueFaxs, and 175.010.2009-023, Zeiss 2p).

Address correspondence to: Nicholas Matthew Bernthal, UCLA Department of Orthopedic Surgery, 1250 16th Street, Suite 3142, Santa Monica, California, 90404, USA. Phone: 424.259.9860; Email: nbernthal@mednet.ucla.edu.

1. Collins I, et al. The diagnosis and management of infection following instrumented spinal fusion. *Eur Spine J*. 2008;17(3):445–450.
2. Sway A, Solomkin JS, Pittet D, Kilpatrick C. Methodology and background for the World Health Organization Global Guidelines on the Prevention of Surgical Site Infection. *Surg Infect (Larchmt)*. 2018;19(1):33–39.
3. Leaper D, et al. Healthcare associated infection: novel strategies and antimicrobial implants to prevent surgical site infection. *Ann R Coll Surg Engl*. 2010;92(6):453–458.
4. Mehta Y, et al. Guidelines for prevention of hospital acquired infections. *Indian J Crit Care Med*. 2014;18(3):149–163.
5. Olsen MA, et al. Risk factors for surgical site infection following orthopaedic spinal operations. *J Bone Joint Surg Am*. 2008;90(1):62–69.
6. Schimmel JJ, Horsting PP, de Kleuver M, Wonders G, van Limbeek J. Risk factors for deep surgical site infections after spinal fusion. *Eur Spine J*. 2010;19(10):1711–1719.
7. Fang A, Hu SS, Endres N, Bradford DS. Risk factors for infection after spinal surgery. *Spine*. 2005;30(12):1460–1465.
8. Rechtine GR, Bono PL, Cahill D, Bolesta MJ, Chrin AM. Postoperative wound infection after instrumentation of thoracic and lumbar fractures. *J Orthop Trauma*. 2001;15(8):566–569.
9. Magill SS, et al. Prevalence of healthcare-associated infections in acute care hospitals in Jacksonville, Florida. *Infect Control Hosp Epidemiol*. 2012;33(3):283–291.
10. Figueiredo AMS, Ferreira FA, Beltrame CO, Côrtes MF. The role of biofilms in persistent infections and factors involved in ica-independent biofilm development and gene regulation in Staphylococcus aureus. *Crit Rev Microbiol*. 2017;43(5):602–620.
11. Oliveira WF, et al. Staphylococcus aureus and Staphylococcus epidermidis infections on implants. *J Hosp Infect*. 2018;98(2):111–117.
12. Levi AD, Dickman CA, Sonntag VK. Management of postoperative infections after spinal instrumentation. *J Neurosurg*. 1997;86(6):975–980.
13. Kowalski TJ, Berbari EF, Huddleston PM, Steckelberg JM, Mandrekar JN, Osmon DR. The management and outcome of spinal implant infections: contemporary retrospective cohort study. *Clin Infect Dis*. 2007;44(7):913–920.
14. Chen SH, Lee CH, Huang KC, Hsieh PH, Tsai SY. Postoperative wound infection after posterior spinal instrumentation: analysis of long-term treatment outcomes. *Eur Spine J*. 2015;24(3):561–570.
15. Kwee TC, Basu S, Alavi A. The ongoing misperception that labeled leukocyte imaging is superior to 18F-FDG PET for diagnosing prosthetic joint infection. *J Nucl Med*. 2017;58(1):182.
16. Termaat MF, Raijmakers PG, Scholten HJ, Bakker FC, Patka P, Haarman HJ. The accuracy of diagnostic imaging for the assessment of chronic osteomyelitis: a systematic review and meta-analysis. *J Bone Joint Surg Am*. 2005;87(11):2464–2471.
17. Bassetti M, et al. 18F-Fluorodeoxyglucose positron emission tomography and infectious diseases: current applications and

future perspectives. *Curr Opin Infect Dis*. 2017;30(2):192–200.
18. Radcliff KE, et al. What is new in the diagnosis and prevention of spine surgical site infections. *Spine J*. 2015;15(2):336–347.
19. Duarte RM, Vaccaro AR. Spinal infection: state of the art and management algorithm. *Eur Spine J*. 2013;22(12):2787–2799.
20. Brown TL, et al. Evaluation of dynamic [18F]-FDG-PET imaging for the detection of acute post-surgical bone infection. *PLoS One*. 2012;7(7):e41863.
21. De Winter F, Vogelaers D, Gemmel F, Dierckx RA. Promising role of 18-F-fluoro-D-deoxyglucose positron emission tomography in clinical infectious diseases. *Eur J Clin Microbiol Infect Dis*. 2002;21(4):247–257.
22. Love C, et al. Diagnosing infection in the failed joint replacement: a comparison of coincidence detection 18F-FDG and 111In-labeled leukocyte/99mTc-sulfur colloid marrow imaging. *J Nucl Med*. 2004;45(11):1864–1871.
23. Berbari EF, et al. Culture-negative prosthetic joint infection. *Clin Infect Dis*. 2007;45(9):1113–1119.
24. Trampuz A, et al. Sonication of removed hip and knee prostheses for diagnosis of infection. *N Engl J Med*. 2007;357(7):654–663.
25. van den Berg S, et al. A human monoclonal antibody targeting the conserved staphylococcal antigen IsaA protects mice against Staphylococcus aureus bacteremia. *Int J Med Microbiol*. 2015;305(1):55–64.
26. Romero Pastrana F, et al. Noninvasive optical and nuclear imaging of Staphylococcus-specific infection with a human monoclonal antibody-based probe. *Virulence*. 2018;9(1):262–272.
27. Dworsky EM, et al. Novel in vivo mouse model of implant related spine infection. *J Orthop Res*. 2017;35(1):193–199.
28. Hu Y, et al. Combinatory antibiotic therapy increases rate of bacterial kill but not final outcome in a novel mouse model of Staphylococcus aureus spinal implant infection. *PLoS One*. 2017;12(2):e0173019.
29. van Oosten M, et al. Real-time in vivo imaging of invasive- and biomaterial-associated bacterial infections using fluorescently labelled vancomycin. *Nat Commun*. 2013;4:2584.
30. Akhtar MS, et al. Antimicrobial peptide 99mTc-ubiquicidin 29-41 as human infection-imaging agent: clinical trial. *J Nucl Med*. 2005;46(4):567–573.
31. Hernandez FJ, et al. Noninvasive imaging of Staphylococcus aureus infections with a nuclease-activated probe. *Nat Med*. 2014;20(3):301–306.
32. Sarda-Mantel L, et al. Evaluation of 99mTc-UBI 29-41 scintigraphy for specific detection of experimental Staphylococcus aureus prosthetic joint infections. *Eur J Nucl Med Mol Imaging*. 2007;34(8):1302–1309.
33. Bardhan NM, Ghosh D, Belcher AM. Carbon nanotubes as in vivo bacterial probes. *Nat Commun*. 2014;5:4918.
34. Panizzi P, et al. In vivo detection of Staphylococcus aureus endocarditis by targeting pathogen-specific prothrombin activation. *Nat Med*. 2011;17(9):1142–1146.
35. van Oosten M, et al. Targeted imaging of bacterial infections: advances, hurdles and hopes. *FEMS Microbiol Rev*. 2015;39(6):892–916.
36. Kaim AH, Weber B, Kurrer MO, Gottschalk J, Von Schulthess GK, Buck A. Autoradiographic quantification of 18F-FDG uptake in experimental soft-tissue abscesses in rats. *Radiology*. 2002;223(2):446–451.
37. De Winter F, Gemmel F, Van De Wiele C, Poffijn B, Uyttendaele D, Dierckx R. 18-Fluorine fluorodeoxyglucose positron emission tomography for the diagnosis of infection in the postoperative spine. *Spine*. 2003;28(12):1314–1319.
38. De Winter F, Huysse W, De Paepe P, Lambert B, Poffyn B, Dierckx R. High F-18 FDG uptake in a paraspinal textiloma. *Clin Nucl Med*. 2002;27(2):132–133.
39. Yamada S, Kubota K, Kubota R, Ido T, Tamahashi N. High accumulation of fluorine-18-fluorodeoxyglucose in turpentine-induced inflammatory tissue. *J Nucl Med*. 1995;36(7):1301–1306.
40. De Winter F, Van De Wiele C, De Clercq D, Vogelaers D, De Bondt P, Dierckx RA. Aseptic loosening of a knee prosthesis as imaged on FDG positron emission tomography. *Clin Nucl Med*. 2000;25(11):923.
41. Brown TL, et al. Evaluation of dynamic [18F]-FDG-PET imaging for the detection of acute post-surgical bone infection. *PLoS One*. 2012;7(7):e41863.
42. Shemesh S, et al. The value of 18-FDG PET/CT in the diagnosis and management of implant-related infections of the tibia: a case series. *Injury*. 2015;46(7):1377–1382.
43. NDA 21-870: FDG F 18 Injection. Food and Drug Administration. https://www.accessdata.fda.gov/drugsatfda_docs/label/2005/021870lbl.pdf. Accessed January 14, 2019.
44. van de Watering FC, Rijpkema M, Perk L, Brinkmann U, Oyen WJ, Boerman OC. Zirconium-89 labeled antibodies: a new tool for molecular imaging in cancer patients. *Biomed Res Int*. 2014;2014:203601.
45. Kahmke R, Moore L, Rosenthal EL, Greene B. Intraoperative fluorescence angiography for head and neck reconstruction. *Curr Otorhinolaryngol Rep*. 2016;4(3):194–200.
46. Schmidt F, Dittberner A, Koscielny S, Petersen I, Guntinas-Lichius O. Feasibility of real-time near-infrared indocyanine green fluorescence endoscopy for the evaluation of mucosal head and neck lesions. *Head Neck*. 2017;39(2):234–240.
47. Pribaz JR, et al. Mouse model of chronic post-arthroplasty infection: noninvasive in vivo bioluminescence imaging to monitor bacterial burden for long-term study. *J Orthop Res*. 2012;30(3):335–340.
48. Francis KP, Joh D, Bellinger-Kawahara C, Hawkinson MJ, Purchio TF, Contag PR. Monitoring bioluminescent Staphylococcus aureus infections in living mice using a novel luxABCDE construct. *Infect Immun*. 2000;68(6):3594–3600.
49. van Dijl JM, et al, inventors; Rijksuniversiteit GroningenAcademisch Ziekenhuis Groningen, assignee. Antibodies Against Staphylococcus Aureus Uses Thereof. US patent application 2017/0002063 A1. January 5, 2017.
50. Stapleton MR, et al. Characterization of IsaA and SceD, two putative lytic transglycosylases of Staphylococcus aureus. *J Bacteriol*. 2007;189(20):7316–7325.
51. Höltje JV, Kopp U, Ursinus A, Wiedemann B. The negative regulator of beta-lactamase induction AmpD is a N-acetyl-anhydromuramyl-L-alanine amidase. *FEMS Microbiol Lett*. 1994;122(1-2):159–164.
52. Loening AM, Gambhir SS. AMIDE: a free software tool for multimodality medical image analysis. *Mol Imaging*. 2003;2(3):131–137.
53. Vosjan MJ, et al. Conjugation and radiolabeling of monoclonal antibodies with zirconium-89 for PET imaging using the bifunctional chelate p-isothiocyanatobenzyl-desferrioxamine. *Nat Protoc*. 2010;5(4):739–743.
54. Perk LR, et al. p-Isothiocyanatobenzyl-desferrioxamine: a new bifunctional chelate for facile radiolabeling of monoclonal antibodies with zirconium-89 for immuno-PET imaging. *Eur J Nucl Med Mol Imaging*. 2010;37(2):250–259.